LAWRENCE
LIVERMORE
NATIONAL
LABORATORY

In-Flight Measurements of Capsule Adiabats in Laser Driven Spherical Implosions

A. L. Kritcher, T. Doppner, C. Fortman, T. Ma, O. L. Landen, R. Wallace, S. H. Glenzer

March 11, 2011

Disclaimer

This document was prepared as an account of work sponsored by an agency of the United States government. Neither the United States government nor Lawrence Livermore National Security, LLC, nor any of their employees makes any warranty, expressed or implied, or assumes any legal liability or responsibility for the accuracy, completeness, or usefulness of any information, apparatus, product, or process disclosed, or represents that its use would not infringe privately owned rights. Reference herein to any specific commercial product, process, or service by trade name, trademark, manufacturer, or otherwise does not necessarily constitute or imply its endorsement, recommendation, or favoring by the United States government or Lawrence Livermore National Security, LLC. The views and opinions of authors expressed herein do not necessarily state or reflect those of the United States government or Lawrence Livermore National Security, LLC, and shall not be used for advertising or product endorsement purposes.

In-Flight Measurements of Capsule Shell Adiabats in Laser Driven Implosions

A. L. Kritcher[1], T. Döppner[1], C. Fortmann[1,2], T. Ma[1], O. L. Landen[1], R. Wallace[1], and S. H. Glenzer[1]

[1]*L-493, Lawrence Livermore National Laboratory, P.O. Box 808, Livermore, CA 94551, USA and*
[2]*Department of Physics and Astronomy, University of California, Los Angeles, CA 90095, USA*
(Dated: March 10, 2011)

We present the first x-ray Thomson scattering measurements of temperature and density from spherically imploding matter. The shape of the Compton downscattered spectrum provides a first-principles measurement of the electron velocity distribution function, dependent on T_e and the Fermi temperature $T_F \sim n_e^{2/3}$. In flight compressions of Be and CH targets reach 6-13 times solid density, with $T_e/T_F \sim 0.4$-0.7, resulting in minimum adiabats of ~ 1.6-2. These measurements are consistent with low-entropy implosions and predictions by simulations using radiation-hydrodynamic modeling.

The study of the microscopic properties of dense matter has gained considerable interest in the last few years, as experiments are underway [1–7] to achieve inertial confinement fusion (ICF) [8, 9] at the National Ignition Facility (NIF) [10]. These experiments are designed to achieve highly compressed states of matter, approaching 1000 g/cc in a cold dense D-T shell surrounding a central hot-spot plasma. The capsule is tuned by shaping the laser power, thereby launching a series of four coalescing shock waves to achieve the desired high fuel densities. The timing and strength of these shocks are important for compressing the solid density target on a low adiabat, i.e., to achieve a low entropy implosion [11]. Furthermore, equation of state measurements at subnuclear densities are important for calculations that model stellar collapse. Here, the entropy per nucleon is conserved to a good approximation and studying the plasma properties of strongly coupled matter along a constant adiabat is of particular interest [12, 13]. Thus, it is important to directly characterize cold and highly compressed plasma states with the goal to validate integrated modeling of spherically imploding matter.

In this letter we present the first simultaneous measurement of the electron density and electron temperature of spherically convergent matter via spectrally resolved x-ray Thomson scattering. We determine in-flight adiabats of 1.6-2, approaching the desired adiabat of 1.5 for implosions driven by shaped laser pulses [14]. While Thomson scattering has previously been applied to planar shock systems [15–21], here we employ high-energy x-rays at ~ 9keV to characterize matter densities of $n_e > 10^{24}$cm^{-3} at the 30 kJ Omega laser facility [22]. Our signal to noise ratio of ~ 200 obtained at these densities indicates the ability for single-shot characterization of imploding targets resulting in a 20% error bar on electron density and temperature. Measurement of the temperature and density enables inferring of the time-resolved CH and Be capsule adiabats, that can be used to test low-adiabat laser pulse shaping [11] and models that predict shock timing for spherically convergent targets.

Probing of the microscopic plasma properties results in both elastic and inelastic scattering features. The intensity of the elastic scattering is sensitive to the static structure factor of the material. The Compton feature provides a direct measure of the electron velocity distribution. For these weakly degenerate plasmas, the velocity distribution is in between a Thomas-Fermi ($T_e = 0$) and a Boltzmann distribution ($T_e >> T_F$). The width of the inelastic Compton feature is sensitive to the Fermi temperature, T_F, which is only dependent on electron density, and the shape of the red wing is sensitive to electron temperature, T_e, [23]. Thus, the temperature and density are simultaneously determined from first principles by accurately measuring the Compton feature width and shape.

Figure 1 shows a schematic of the experimental configuration. In these experiments, CH and Be capsules (outer diameter = 860μm, $\rho_{o,Be}$=1.85 g cm^{-3}, $\rho_{o,CH}$=1.1 g cm^{-3}, 40-45 μm thick) have been compressed and heated in a spherical geometry by ~ 15kJ of 351-nm laser light. The laser light was delivered by 36 shaped drive beams (with ~ 0.6 TW in a 1ns foot and ~ 15 TW in a 1ns peak, see Fig.1) [24–26]. Self emission from the capsules enables probing of the shell radius for $t < 2.9$ ns. Also shown in Fig. 1 are measured radii overlaid on radiation hydrodynamic simulations of the shell mass density as function of time and shell radius. Here, $t = 0$ns denotes the start of the drive beams. At $t = 2$ns when the laser pulse has turned off, self-emission images of the imploding shells become extremely noisy, lending to the larger error bars. At $t > 2.9$ns, no images could be recorded. In order to enable probing of extremely high energy density conditions later in the implosion and to measure the adiabat, we employ x-ray Thomson scattering [15].

To characterize the compressed shells with x-ray scattering, a laser-produced zinc He-α x-ray source delayed in time from the compression beams was scattered from the targets at 135$\pm$15°, accessing the non-collective regime. The Zn He-α x-ray source (9keV) was produced using
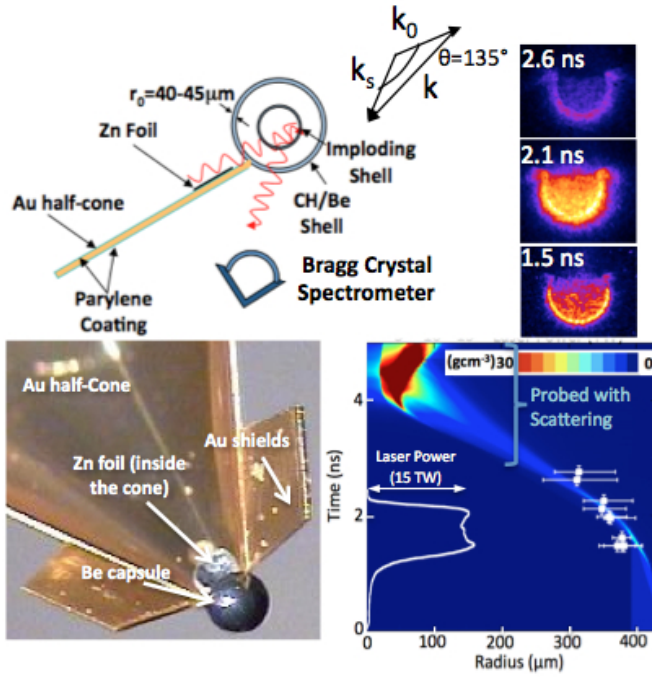
FIG. 1: Schematic of the experimental set-up: (top left) detailed illustration of the target with a view perpendicular to the scattering plane (bottom left) photo of a Be cone-in-half-shell target. Here, Zn He-α x rays, produced via laser irradiation of a $10\mu m$ thick Zn foil mounted inside a gold cone, are scattered at θ=135° from imploding Be and CH capsules. (top right) Self-emission images of imploding Be shells at 1.7, 2.1, and 2.9 ns after the start of the drive beams. (bottom right) Radiation-hydrodynamic simulations of the imploding shell mass density as a function of radius and time. The overlaid white data points are measured radii from self-emission images and the white curve is the laser power profile as a function of time.

7-9 additional shaped laser beams (5.5×10^{15}Wcm^{-2}, see Fig.1) that irradiated $10\mu m$ thick Zn foils, mounted onto gold half-cones attached to the capsules. The gold cones (length 7mm, $60\mu m$ thick, 60° opening) ensured that the crystal spectrometer detected only scattered x-rays from the implosion. Additional gold shields were used to block potential Zn emission from plasma expansion around the cone. The gold cones and shields were coated with $10\mu m$ thick parylene to reduce bremsstrahlung emission from hot electrons. The scattered x-rays were measured using a high efficiency, high energy resolution HOPG crystal spectrometer coupled to an x-ray framing camera with a gate time of 180 ps and a CCD detector. Additional diagnostics include a streaked crystal spectrometer used to measure the Zn probe emission as a function of time for each shot, and pinhole cameras that yield temporally resolved images of the ablator emission during the drive laser pulse.

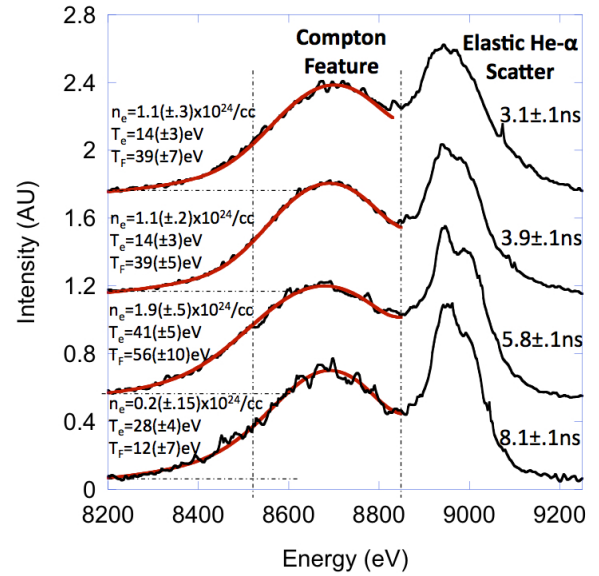In these experiments non-collective behavior of the

FIG. 2: Measured (black) and best fits (red) to the Compton feature of the scattered spectra from Be implosions at various times, yielding n_e and T_e. The data show elastic scattering at 9 keV and downshifted inelastic Compton scattering.

plasma was measured, where the scattering parameter $\alpha_e = 1/k\lambda_S = hc/(E_0 2\pi\lambda_S) < 1$. Here, k is the magnitude of the scattering vector, where $k = (4\pi E_0/hc)\sin(\theta_s/2)$, and λ_S is the screening length. The scattering regime can be set by choosing the energy of the incident probe x-rays, E_0, and the angle of the detected scattered x-rays, θ_s. For the conditions in this experiment, E_0=9 keV and θ_S=135 ± 15°, the scattering parameter $\alpha_e \sim 0.27$.

Figure 2 shows measured x-ray scattering spectra from spherically driven Be capsules at t=3.1±0.1 ns and 3.9±0.1 ns, before maximum convergence, at t=5.7±0.1 ns, about the time of maximum convergence, and t=8.1±0.1ns, after maximum convergence. We observe elastic scattering at $\sim$ 9 keV and inelastic Compton scattering at $\sim$ 8.7 keV. The Compton feature is down-shifted by the Compton energy, $\Delta E_C \sim 260eV$, and spectrally broadened by the electron velocity distribution due to Doppler shifting in the field of view of the detector For our conditions of a weakly degenerate plasma, the width of the Compton feature is mainly sensitive to changes in the Fermi energy ($T_F^{1/2} \sim n_e^{1/3}$). The shape of the red wing is used to extract additional information on T_e. In these experiments the high signal to noise of our data enables highly resolved measurements of the Compton red wing shape, thus allowing us to obtain a model-independent measure of T_e from the electron velocity distribution.

At t=3.1±0.1 and t=3.9±0.1ns the best theoretical fits of the electron velocity distribution to the experimental

Compton spectra yield $T_e=(14\pm3)$ eV, $n_e=(1.1\pm0.2)\times10^{24}$cm^{-3}, and Be(+2). For scattering at t=5.8±0.1 ns, fits indicate near peak compression with $n_e=(1.9\pm0.5)\times10^{24}$cm^{-3}, and Be(+2.5), i.e. 6(±1.5)x solid density, and $T_e=(41\pm5)$ eV. At t=8.1±0.1 ns the temperature and density decrease to $(24\pm2)eV$, $n_e=(0.2\pm.15)\times10^{24}$cm^{-3}, and Be(+2) indicating that the shell is hydrodynamically expanding and cooling. The ionization state has been measured within an error of 25% from the scattering of weakly bound electrons resulting in an inelastic feature shifted beyond the red wing of the Compton feature. These measurements are consistent with previous Be ionization data at similar temperatures [15]. For CH, the ionization state is determined within an error of 20%, in agreement with previous CH ionization data at similar temperatures [27].

In Fig. 3 (top), RMS values of theoretical fits to the experimental data at t=3.9±0.1ns show an accuracy of ~20% in determining the electron density and temperature ($T_e=T_i$) from the shape of the electron velocity distribution. The dark island in the center of the plot is the range of best fits to the experimental data. Figure 3 (bottom) shows experimental data at t=3.9±0.1ns plotted with calculations of the Thomson scattered spectra for varying T_e and n_e. Fig. 3 a) shows sensitivity of the Compton feature red wing to changes in T_e for a fixed electron density and ionization state of 1.1×10^{24}cm^{-3} and Be(+2). Shown in Fig. 3 b) is the sensitivity of the Compton feature width to electron density for a fixed electron temperature of 14 eV and ionization state of Be(+2). Fig. 3 (bottom) shows fitting to the data that becomes too steep c) and too parabolic d) to fit the slope of the Compton feature red wing, as T_e and n_e are simultaneously varied. These plots show that if either n_e or T_e is known, the other parameter can be determined within ±5%. However, determining both n_e and T_e from the Compton spectra, yields error bars are ±20%.

Temporally resolved measurements of the electron temperature, electron density, and ionization state enable determining of the adiabat, defined as the ratio of total electron and ion pressure to electron Fermi pressure, given to within a few percent for $T_e < T_F$ and to better than 10 percent for $T_e > T_F$ as

$$\alpha = \frac{n_e(3/5)\sqrt{(1+8.2(T_e/T_F)^2)}+n_iT_i}{n_e(3/5)T_F}. \quad (1)$$

Here, T_e, T_i, and T_F are the electron temperature, ion temperature, and $T_F\sim n_e^{2/3}$, respectively. We assume that the electron and ion temperatures are equal in these strongly collisional plasmas.

Figure 4 shows the adiabat for spherically compressed CH and Be shells. Also plotted are 1D radiation-hydrodynamic simulations of the adiabat as a function of time using HELIOS [28]. The simulation bands reflect the minimum predicted adiabat (lower bound) and
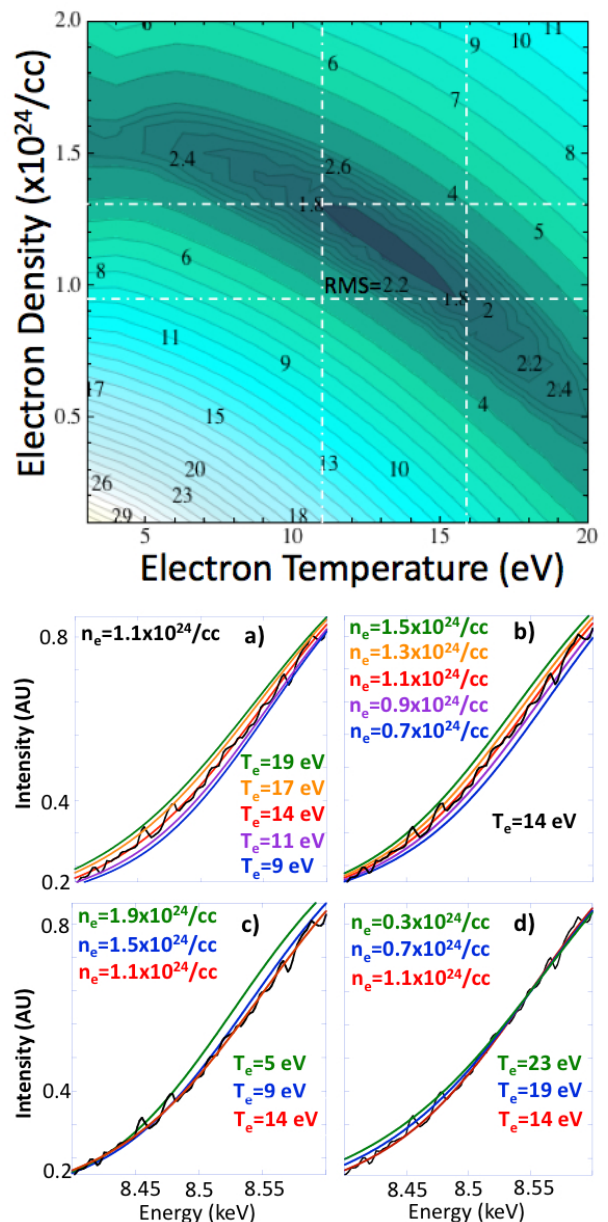

FIG. 3: (top) Example of RMS fits of the experimental Compton feature for Be scattering data taken at 3.9±0.1ns. The dark colored island in the center of electron temperature and density space is a range of best fits to the experimental data. (bottom) Fits plotted together with the measured Compton red wings for varying electron temperature and density, indicating an accuracy of ±20%.

density and temperature weighted adiabat over the compressed shell region that contributes to the scattering spectra (upper bound). The error bars of the measured adiabats reflect the error in determining electron temperature, electron density, and ionization state, see Fig. 3.

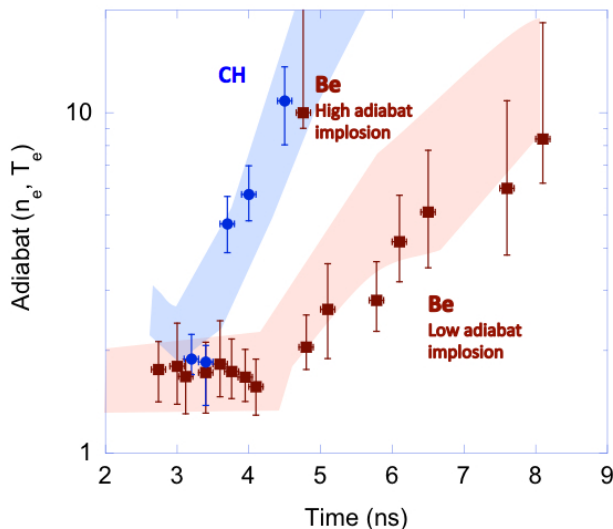While the in-flight adiabats for Be and CH are similar, the CH capsules reach compressions of up to 12x

FIG. 4: Adiabat plotted as function of time for compressed Be and CH ablators. Also plotted are 1D radiation-hydrodynamic calculations. The bands reflect partial scattering from the low-density blow-off plasma in addition to the compressed region.

solid density, whereas the maximum observed Be capsule compression is 6x solid density. Higher CH densities are reached by compressing a lower initial mass (0.9×10^{-4}g) than for the Be capsules (1.8×10^{-4}g) with the same laser drive conditions. The steep adiabat increase after maximum convergence happens earlier for CH than for Be, as expected for compressing lower density capsules with the same drive parameters. The simulated timing of the adiabat increase roughly agrees with experimental measurements for Be. However, simulations of the compressed CH capsules predict a slower expansion than the experimental measurements suggest. A near optimum adiabat of α=1.5, necessary for ignition, can be reached for both CH and Be with the pulse shaping described in this work. In contrast, when the laser drive conditions are untuned, e.g. using a similar pulse shape with only ∼40% of the drive energy and a peak-to-foot intensity ratio of ∼125 compared to ∼27 used in this work, the Be capsule in-flight adiabat increases to ≥9, also shown in Fig.4.

In summary, we have accurately measured the model independent temperature and density of highly compressed targets, $n_e > 10^{24}$cm^{-3}. We have also measured the adiabat of spherically compressed CH and Be capsules. These measurements show that the adiabat can be tuned for both CH and Be to the near optimum levels needed for ignition through laser pulse shape tuning. High-quality data obtained in these experiments indicates the ability for single-shot characterization of ICF targets. The signal to noise ratio of the data ∼ 200 provides a basis for future adiabat and dense matter studies of high density matter using this platform. In addition, information on the elastic scattering component for well defined density and temperature conditions will enable future tests of dense matter structure factor models.

[1] J. L. Kline *et al.*, Phys. Rev. Lett. **106**, 085003 (2011).
[2] S. H. Glenzer *et al.*, Phys. Rev. Lett. **106**, 085004 (2011).
[3] S. H. Glenzer *et al.*, Science **327**, 1228 (2010).
[4] E. L. Dewald *et al.*, Rev. Sci. Instrum. **81**, 10D938 (2010).
[5] P. Michel *et al.*, Phys. Rev. Lett. **102**, 025004 (2009).
[6] N. B. Meezan *et al.*, Phys. Plasmas **17**, 056304 (2010).
[7] G. A. Kyrala *et al.*, Rev. Sci. Instrum. **81**, 10E316 (2010).
[8] J. Nuckolls *et al.*, Nature, **239** (1972).
[9] J. D. Lindl *et al.*, Phys. Plasmas **11**, 339. (2004).
[10] E. I. Moses *et al.*, Phys. Plasmas **16**, 041006 (2009).
[11] S. W. Haan *et al.*, Nucl. Fusion **44**, S171 (2004).
[12] S. Marcos *et al.*, Nucl. Phys. A, **381**, 507 (1982).
[13] C. J. Pethick *et al.*, Nucl. Phys. A, **414**, 517 (1984).
[14] Phys. Plasmas, *in progress*, (2011).
[15] S. H. Glenzer and R. Redmer, Rev. Mod. Phys. **81**, 1625 (2009).
[16] G. Gregori *et al.*, Phys. Rev. Lett. 101, 045003 (2008).
[17] H. J. Lee *et al.*, Phys. Rev. Lett. **102**, 115001 (2009).
[18] E. Garcia Saiz *et al.*, Nature Physics **4**, 940 (2008).
[19] A. L. Kritcher *et al.*, Science, **322**, 69 (2008), *ibid* Phys. Plasmas **16**, 056308 (2009).
[20] B. Barbrel *et al.*, Phys. Rev. Lett. **102**, 165004 (2009).
[21] D. Riley *et al.*, Phys. Rev. Lett. **84**, 8 (2000).
[22] J. M. Soures *et al.*, Fusion Technol. **30**, 492 (1996).
[23] O. L. Landen *et al.*, J. Quant. Spectrosc. Radiat. Transf. **71**, 465 (2001).
[24] C. Zhou *et al.*, Phys. Rev. Lett. **98**, 025044 (2007).
[25] W. Theobald *et al.*, Plasma Phys. Control. Fusion **51**, 124052 (2009).
[26] C. Stoeckl *et al.*, Plasma Phys. Control. Fusion **50**, 124044 (2008).
[27] G. Gregori *et al.*, J. Quant. Spectrosc. Radiat. Transfer, **99**, 225 (2006).
[28] J. J. MacFarlane *et al.*, JQSRT **99**, 381-397 (2006).